



Dynamic supercoiling bifurcations of growing elastic filaments

Charles W. Wolgemuth^a, Raymond E. Goldstein^b, Thomas R. Powers^{c,*}

^a Department of Cell Biology, University of Connecticut Health Center, Farmington, CT 06030, USA

^b Department of Physics and Program in Applied Mathematics, University of Arizona, Tucson, AZ 85721, USA

^c Division of Engineering, Brown University, Box D, Providence, RI 02912, USA

Received 12 April 2003; received in revised form 5 September 2003; accepted 16 October 2003

Communicated by E. Bodenschatz

Abstract

Certain bacteria form filamentous colonies when the cells fail to separate after dividing. In *Bacillus subtilis*, *Bacillus thuringiensis*, and *Cyanobacteria*, the filaments can wrap into complex supercoiled structures as the cells grow. The structures may be solenoids or plectonemes, with or without branches in the latter case. Any microscopic theory of these morphological instabilities must address the nature of pattern selection in the presence of *growth*, for growth renders the problem nonautonomous and the bifurcations dynamic. To gain insight into these phenomena, we formulate a general theory for growing elastic filaments with bending and twisting resistance in a viscous medium, and study an illustrative model problem: a growing filament with preferred twist, closed into a loop. Growth depletes the twist, inducing a twist strain. The closure of the loop prevents the filament from unwinding back to the preferred twist; instead, twist relaxation is accomplished by the formation of supercoils. Growth also produces viscous stresses on the filament which even in the absence of twist produce buckling instabilities. Our linear stability analysis and numerical studies reveal two dynamic regimes. For small intrinsic twist the instability is akin to Euler buckling, leading to solenoidal structures, while for large twist it is like the classic writhing of a twisted filament, producing plectonemic windings. This model may apply to situations in which supercoils form only, or more readily, when axial rotation of filaments is blocked. Applications to specific biological systems are proposed.

© 2003 Elsevier B.V. All rights reserved.

PACS: 87.17.-d; 87.16.Ka; 05.45.-a; 46.70.De

Keywords: Supercoil; Growth; Elastic filaments; Filamentous bacteria

1. Introduction

Many structures in the biological world grow so slowly that they adopt a shape that can be considered as a minimizer of some configurational energy associated solely with the *internal* structure. The logarithmic spiral of the nautilus shell is an example. It enlarges through a process of differential growth whereby its shape represents the accumulated history of identical events, save for scale changes [1]. Thus, the microscopic rules of growth are

* Corresponding author. Tel.: +1-4018632868; fax: +1-4018639009.

E-mail addresses: cwolgemuth@uchc.edu (C.W. Wolgemuth), gold@physics.arizona.edu (R.E. Goldstein), thomas_powers@brown.edu (T.R. Powers).

essentially unchanging as the three-dimensional form develops, and the properties of the external environment do not fundamentally determine the form.

Environmental effects on the development of biological forms are well known. Consider the formation of tendril perversions in climbing vines [2,3]. A perversion is a junction between regions of opposite helix handedness that forms as an initially straight tendril first attaches to a support structure and then, through the activation of tension-sensitive receptors, undergoes a helical instability. The constraint of fixed ends enforces the formation of a structure with zero net twist, consisting of concatenated regions of opposite chirality joined by a transition region—the perversion. Thus, the interaction with the external environment fundamentally alters the pattern formation through the tension induced by a point contact.

Even more complex phenomena occur for those structures whose very process of growth induces an *external* force, as with motion through an environment that offers viscous resistance. These new forces can dramatically alter the ultimate configuration, and the present paper is a case study in such phenomena. We focus on a system in which the formation of patterns occurs through a finite-wavelength instability in which the process of growth introduces an intrinsic time-dependence to the control parameters. The resulting bifurcation problem is nonautonomous and can exhibit a rich phenomenology as the intrinsic time scale of growth competes with those of the various modes of instability. This competition places the problem among the class of so-called “dynamic bifurcations”, of which many examples are of continuing interest. These include instabilities in directional solidification in which the initial acceleration of the interface from rest provides the nonautonomous character [4], fingering instabilities of magnetic fluids under the influence of time-dependent magnetic fields [5,6], and separatrix crossing in Hamiltonian systems viewed as models for stellar fission [7].

Motivation for this focus comes from the phenomenon of supercoiling exhibited by filamentous colonies of *Bacillus subtilis* and other bacteria. *B. subtilis* cells are rod-shaped bacteria, typically 4 μm in length and slightly over 1.5 μm in diameter. Wild-type rod-shaped bacteria grow by extending along the cylindrical axis of symmetry, and then dividing and separating in the middle [8,9]. Under certain conditions, the cells of some mutant forms fail to separate upon replication, leading to a long chain of cells. Other species have also been observed to form chains, including *Escherichia coli* [10], *Cyanobacteria* [11], *Myxococcus xanthus* [12], and *Mycobacterium tuberculosis* [13]. Under certain growth conditions, strains of *B. subtilis*, *Bacillus stearothermophilus* [14], *Thermus* [15], and *Mastigocladus laminosus* [16] form complex braided structures. Helical (or, in the jargon of DNA biophysics, “solenoidal”) morphologies have also been observed [17]. Of these examples, the supercoiled structures of *B. subtilis* have been studied most extensively [18,19]. Recent experimental work [20,21] has indicated that the cell wall of *B. subtilis* contains helical protein structures. These may supply the molecular imprinting responsible for this morphological development, in a manner analogous to the way microtubules control macroscopic handedness in certain plants [22], but as of yet no successful microscopic theory for the formation of these supercoiled structures exists.

Throughout much of the development of complex structures in *B. subtilis*, the length L of the elongating chain, a single cell thick, grows exponentially in time, $L \propto \exp(\sigma t)$, with the growth rate $\sigma \approx 2 \times 10^{-4} \text{ s}^{-1}$. Moreover, material cross-sections of the cells rotate relative to each other [23], so that the angle describing the relative orientation of any two material cross-sections is proportional to their exponentially increasing separation. In one of the earliest observations of supercoiling in *B. subtilis*, the ends of the fiber adhered to a spore coat, prohibiting axial rotation of the ends [18]. Mendelson [18] supposed that this blocked rotation leads to torsional stress, eventually causing supercoiling (see Fig. 1). Since this discovery, it has been shown that adhesion is not required for supercoiling [19], and that many different factors such as temperature, pH, and the concentration of ions such as magnesium and ammonium affect the morphology of the coils [24,25]. The evolution of the coils after the formation of the first braid is remarkable. The first plectonemic braid, essentially a filament that is two cells thick, continues to grow and eventually reaches a critical length of order 100 μm , after which it supercoils to form another braided structure which is four cells thick. This process can repeat many times, leading to a hierarchy of braids and eventually a macroscopic object.

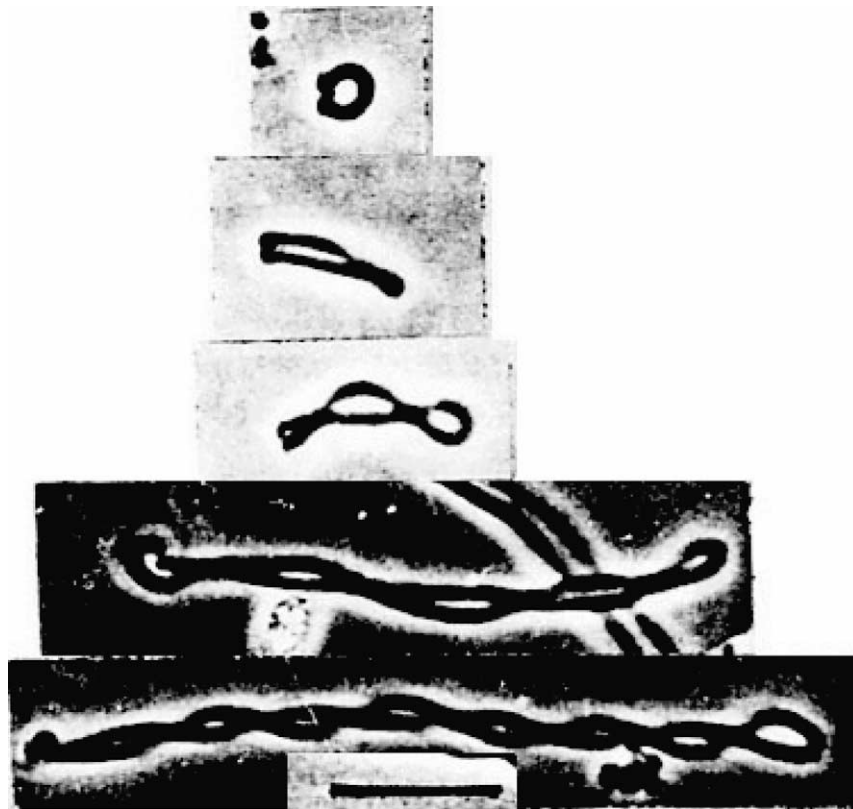


Fig. 1. Phase contrast micrographs of growing *B. subtilis* spores with attachment of both cell poles to the spore coat. The series consists of different filaments at various stages of growth. Scale bar = 10 μm . Figure courtesy of N. Mendelson; see [18].

In this paper, we study in detail Mendelson's blocked rotation mechanism of supercoiling in a growing closed loop, and focus on the formation of the initial braid. While not yet explaining the microscopic physical origin of the coiling instability, we elucidate the rich dynamics that occurs when growth competes with blocked rotation, and thereby help constrain more detailed theories.

With this focus we exploit several simplifying assumptions in our analysis. First, the chain of cells is treated as an elastic filament with uniform properties along its length. There is evidence that this assumption holds until times comparable to a few doubling times ($\sim\sigma^{-1}$), but may be violated later. For example, when the chirality of nutrient molecules in the growth medium is reversed, the supercoils unwind and even begin to wrap up in the opposite handedness, but the hairpin bends from the original braid remain [26]. Thus, some of the deformation of the growing filament becomes permanent. This phenomenon is reminiscent of the morphological development of plant tendrils, in which young and flexible tendrils age with time, becoming woody and locked in a fixed shape [27]. On the time scales that will concern us, $t \lesssim \sigma^{-1}$, single fibers have been shown to behave like elastic rods, with a bending modulus $A = 10^{-12}$ erg cm [28], as discussed further in Section 2.4.

A second major simplification we introduce is to treat the growth rate as constant in time, independent of stress and filament geometry. Again, the permanent hairpin bends in the chirality reversal experiment show that this assumption cannot hold everywhere along the filament for all times after the first braid forms.

Together with the observation that viscous effects dominate inertial effects in the low Reynolds number environment of the growing fibers, these assumptions lead to the model studied in this paper: an elastic ring with intrinsic

twist suspended in a viscous fluid and lengthening at an exponential rate. Our work is complementary to that of other investigators. For example, Shelley and Ueda [29] studied the Euler-like buckling of a growing liquid crystal filament, using a local drag model for the linear stability of a growing loop, and incorporating nonlocal Stokesian hydrodynamics to study the pattern formation [30]. Drasdo [31] studied similar patterns in the context of the growth of single-cell-layer tissue sheets. Klapper [32] has studied inertial writhing instabilities of *open* rods subject to exponential growth, as well as the relaxation to equilibrium of twisted rings in the absence of growth. Goriely and Tabor [33] introduced the idea of *twist depletion* as a possible mechanism driving buckling in *B. subtilis*.

Our analysis begins with a generalization of the kinematics and dynamics of slender filaments to account for growth. Section 3 treats the growing elastic loop, beginning with a qualitative discussion of the instability. The linear stability analysis is greatly simplified by the use of the natural frame, so in this section we include a self-contained summary of the properties of the natural frame. We present a quasi-analytic treatment of the linear stability of the loop, and then present numerical simulations of the full nonlinear problem. Section 4 is the conclusion.

2. Kinematics and dynamics of growing rods

2.1. Centerline kinematics

In this section we extend the standard kinematics and dynamics of elastic rods to allow for growth. Let s denote the arclength measured at time t from one end of an open rod, or from a fixed material point for a rod closed to form a loop. Then $\mathbf{r}(s, t)$ is the position in space of the centerline of the rod with arclength coordinate s at time t . Since material points on the rod centerline are convected along the rod by growth, fixed values of s do not correspond to fixed material points. We choose to label the material points of the centerline at all times by the arclength parameterization s_0 at a fixed time $t = 0$. We will study exponential growth, for which $s = \exp(\sigma t)s_0$. Note that the partial derivatives with respect to s and t commute because s and t are independent variables:

$$\left. \frac{\partial}{\partial t} \right|_s \left. \frac{\partial}{\partial s} \right|_t = \left. \frac{\partial}{\partial s} \right|_t \left. \frac{\partial}{\partial t} \right|_s, \quad (1)$$

however, $\partial/\partial t|_{s_0}$ and $\partial/\partial s|_t$ do not commute since

$$\left. \frac{\partial}{\partial t} \right|_{s_0} = \left. \frac{\partial}{\partial t} \right|_s + \left. \frac{\partial s}{\partial t} \right|_{s_0} \left. \frac{\partial}{\partial s} \right|_t \quad (2)$$

by the chain rule.

The velocity of a material point is the time derivative of position at fixed s_0 :

$$\mathbf{v}(s_0, t) = \left. \frac{\partial \mathbf{r}}{\partial t} \right|_{s_0}. \quad (3)$$

It is convenient to develop the equations of motion in terms of s rather than s_0 , so that

$$\mathbf{v}(s, t) = \left. \frac{\partial \mathbf{r}}{\partial t} \right|_s + \left. \frac{\partial s}{\partial t} \right|_{s_0} \left. \frac{\partial \mathbf{r}}{\partial s} \right|_t. \quad (4)$$

To avoid confusion, we will explicitly denote which variables are fixed when finding the partial derivatives with respect to t . However, since partial derivatives with respect to s will always be taken at fixed t , we will write $\partial/\partial s|_t = \partial/\partial s$.

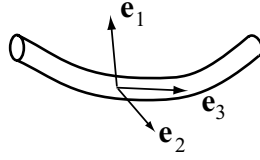


Fig. 2. The material frame. The unit vector $\hat{\mathbf{e}}_3$ is tangent to the rod centerline. The other members of the orthonormal frame, $\hat{\mathbf{e}}_1$ and $\hat{\mathbf{e}}_2$, point to material points on the rod's surface.

The first term of Eq. (4) corresponds to the velocity of the centerline in the absence of growth, and the second term arises from growth-induced convection. Henceforth we will specialize to exponential growth, for which $\partial s / \partial t|_{s_0} = \sigma s$ and

$$\mathbf{v} = \frac{\partial \mathbf{r}}{\partial t} \Big|_s + s\sigma \frac{\partial \mathbf{r}}{\partial s} = \frac{\partial \mathbf{r}}{\partial t} \Big|_s + s\sigma \hat{\mathbf{e}}_3, \quad (5)$$

where $\hat{\mathbf{e}}_3 = \partial \mathbf{r} / \partial s$ is the unit tangent vector of the centerline. Although the velocity of a material point may seem from Eq. (5) to depend on the arbitrary choice of origin for s , Eq. (3) shows that the velocity is manifestly independent of this choice. Note that Eq. (5) implies that $\hat{\mathbf{e}}_3 \cdot \partial \mathbf{v} / \partial s = \sigma$.

2.2. Choice of frame and growth model

In Kirchhoff rod theory [34], the configuration of a rod is completely specified by the orientation of the material orthonormal frame $\{\hat{\mathbf{e}}_1, \hat{\mathbf{e}}_2, \hat{\mathbf{e}}_3\}$. The vectors $\hat{\mathbf{e}}_1$ and $\hat{\mathbf{e}}_2$ point to material points on the rod surface (Fig. 2). As the rod bends and twists, the positions of these material points change, causing the material frames to rotate [35]:

$$\frac{\partial \mathbf{e}_i}{\partial s} = \boldsymbol{\Omega} \times \mathbf{e}_i, \quad (6)$$

$$\frac{\partial \mathbf{e}_i}{\partial t} \Big|_{s_0} = \boldsymbol{\omega} \times \mathbf{e}_i. \quad (7)$$

The vector $\boldsymbol{\Omega}$ describes the bending and twisting strain at a given instant, and $\boldsymbol{\omega}$ is the angular velocity of a material frame at a given material point s_0 . In general, $\boldsymbol{\Omega}$ and $\boldsymbol{\omega}$ depend on the choice of material frame. Once the choice is made for a given configuration, say the stress-free state, then the choice is specified for all configurations. In the classical rod theory without growth, it is natural to align $\hat{\mathbf{e}}_1$ and $\hat{\mathbf{e}}_2$ with the principal axes of the cross-section. If the cross-section is circular, as we henceforth assume, and if the rod is straight in the absence of stress, then there are many equivalent natural choices. For example, if the rod aligns along the z -axis when it is stress-free, then $\{\hat{\mathbf{e}}_1, \hat{\mathbf{e}}_2\} = \{\hat{\mathbf{x}}, \hat{\mathbf{y}}\}$ is natural. Any uniform rotation of this frame about $\hat{\mathbf{z}}$ is equally convenient; all these choices lead to $\boldsymbol{\Omega} = 0$ in the absence of stress.

If the rod is curved in the stress-free state, then the direction of curvature breaks the rotational symmetry of the circular cross-section and provides a natural choice for the directions of $\hat{\mathbf{e}}_1$ and $\hat{\mathbf{e}}_2$, e.g. if the rod has a helical stress-free state, then we may take $\hat{\mathbf{e}}_1 = \hat{\mathbf{n}}$ and $\hat{\mathbf{e}}_2 = \hat{\mathbf{b}}$, where $\hat{\mathbf{n}}$ and $\hat{\mathbf{b}}$ are the unit normal and binormal of the Frenet–Serret frame [36–38], respectively:

$$\frac{\partial \hat{\mathbf{e}}_3}{\partial s} = \kappa \hat{\mathbf{n}}, \quad (8)$$

$$\frac{\partial \hat{\mathbf{n}}}{\partial s} = -\kappa \hat{\mathbf{e}}_3 + \tau \hat{\mathbf{b}}, \quad (9)$$

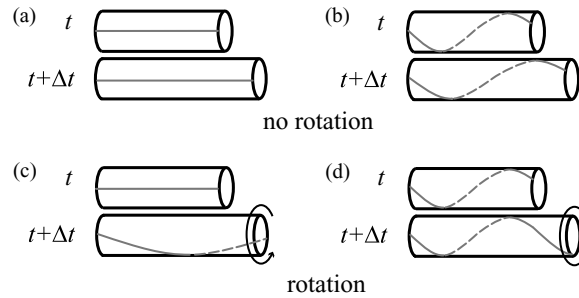


Fig. 3. Two different modes of growth. In (a) and (b), the rod lengthens without rotation. In (c) and (d), cross-sections at fixed material points rotate with an ever-increasing angular velocity.

$$\frac{\partial \hat{\mathbf{b}}}{\partial s} = -\tau \hat{\mathbf{n}}, \quad (10)$$

where κ is the curvature and τ the torsion. Thus, $\mathbf{\Omega} = \kappa_0 \hat{\mathbf{e}}_2 + \tau_0 \hat{\mathbf{e}}_3$ for this frame in the absence of stress, where κ_0 is the curvature and τ_0 the torsion of the helix.

When $\kappa_0 = 0$, the helix of the last example degenerates to a straight rod with spontaneous twist τ_0 . We will show below that if $\kappa_0 = 0$ and the cross-section is circular, then τ_0 can be eliminated from the equations of motion for an inextensible (non-growing) rod, and therefore does not affect the rod shape and dynamics. However, τ_0 has physical meaning for a *growing* rod, even if $\kappa_0 = 0$ and the cross-section is circular. Fig. 3 illustrates two kinematic possibilities for growth. Each sub-figure shows the stress-free configuration of a growing rod at two different times. In all cases, the left end of the rod has a fixed position and orientation. Two growth schemes are shown; in the growth scheme of Fig. 3a and b, the material frames are carried to greater values of z by growth and have no angular velocity. A line of material points parallel to the z -axis at time t remains parallel to the z -axis at time $t + \Delta t$ (Fig. 3a). However, the pitch of a *helical* line of material points increases as the filament grows (Fig. 3b). Since the angular velocity is zero, the number of helical turns is constant.

Fig. 3c and d illustrates a growth scheme in which the cross-sections rotate with an angular velocity that increases with arclength. In this case, a line of material points parallel to the z -axis at time t wraps around the rod at time $t + \Delta t$ (Fig. 3c). As the rod grows, the material frames are carried to greater values of z but also *rotate* relative to the fixed frame at $s = 0$. In this paper, we will study the growth model of Fig. 3c and d since it describes the relative rotation of the cross-sections of the *B. subtilis* fibers [39,40]. Define $\theta(s_0) = \cos^{-1}(\hat{\mathbf{e}}_1(0) \cdot \hat{\mathbf{e}}_1(s_0))$ as the angle between the orientation of the (zero-stress) material frames at s_0 and $s = 0$. We will suppose that $\theta(s_0)$ increases linearly with s_0 and exponentially in time with rate σ :

$$\theta(s_0) = \tau_0 s_0 \exp(\sigma t) = \tau_0 s. \quad (11)$$

Since $\theta(s_0, t)$ and $s(s_0, t)$ increase in time with the same exponential rate, a helical material line on the rod surface with pitch $2\pi/\tau_0$ remains a helical line with the same pitch as time passes (Fig. 3d). Thus, the natural choice for the material frame in the stress-free state is

$$\hat{\mathbf{e}}_1 = \cos(s\tau_0) \hat{\mathbf{x}} + \sin(s\tau_0) \hat{\mathbf{y}}, \quad (12)$$

$$\hat{\mathbf{e}}_2 = -\sin(s\tau_0) \hat{\mathbf{x}} + \cos(s\tau_0) \hat{\mathbf{y}}, \quad (13)$$

$$\hat{\mathbf{e}}_3 = \hat{\mathbf{z}}. \quad (14)$$

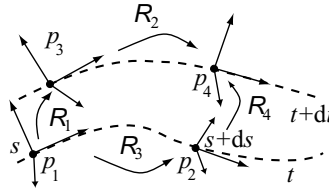


Fig. 4. Geometrical origin of compatibility relations.

Note that $\mathbf{\Omega} = \tau_0 \hat{\mathbf{e}}_3$ and $\boldsymbol{\omega} = \sigma \tau_0 \hat{\mathbf{e}}_3$ for this frame; $\boldsymbol{\omega} \neq 0$ since the material frames must rotate to maintain zero-stress as the rod grows (in contrast to the growth model of Fig. 3a). The parameter τ_0 not only characterizes the configuration of the natural material frame (as in the inextensible helix example) but also the mode of growth.

2.3. Compatibility relations

Geometry relates the strain vector $\mathbf{\Omega}$ and the angular velocity $\boldsymbol{\omega}$. To see how, consider Fig. 4. The lower curve represents the centerline of the rod at time t , and the upper curve represents the centerline of the rod at time $t + dt$. The labeled points on the upper curve have the same material coordinate as the corresponding points on the lower curve; thus, the arclength parameter for p_3 is $s \exp(\sigma dt) \approx s + s \sigma dt$, while the arclength parameter for p_4 is $(s + ds) \exp(\sigma dt) \approx (s + ds)(1 + \sigma dt)$. Let \mathbf{R}_1 be the rotation matrix carrying the frame at p_1 to p_3 , \mathbf{R}_2 the rotation matrix carrying the frame at p_3 to p_4 , \mathbf{R}_3 the rotation matrix carrying the frame at p_1 to p_2 , and \mathbf{R}_4 the rotation matrix carrying the frame at p_2 to p_4 . Furthermore, let \mathbf{J} and \mathbf{K} denote the infinitesimal rotation matrices associated with the rotation vectors $\mathbf{\Omega}$ and $\boldsymbol{\omega}$, respectively (e.g. $J_{\alpha\beta} = \epsilon_{\alpha\beta\gamma} \Omega_\gamma$, where $\epsilon_{\alpha\beta\gamma}$ is the alternating symbol). From the definitions of the rotation matrices, $\mathbf{R}_2 \mathbf{R}_1 = \mathbf{R}_4 \mathbf{R}_3$, or

$$[\mathbf{I} + (1 + \sigma dt) ds \mathbf{J}(s + s\sigma dt, t + dt)][\mathbf{I} + dt \mathbf{K}(s, t)] \approx [\mathbf{I} + dt \mathbf{K}(s + ds, t)][\mathbf{I} + ds \mathbf{J}(s, t)], \tag{15}$$

where \mathbf{I} is the identity matrix. Expanding Eq. (15) to $\mathcal{O}(ds dt)$, we find

$$\frac{\partial \mathbf{K}}{\partial s} = \frac{\partial \mathbf{J}}{\partial t} \Big|_s + \sigma s \frac{\partial \mathbf{J}}{\partial s} + \sigma \mathbf{J} + [\mathbf{J}, \mathbf{K}], \tag{16}$$

$$\frac{\partial \mathbf{K}}{\partial s} = \frac{\partial \mathbf{J}}{\partial t} \Big|_{s_0} + \sigma \mathbf{J} + [\mathbf{J}, \mathbf{K}], \tag{17}$$

where $[\cdot, \cdot]$ is the commutator. In terms of components in the material frame:

$$\frac{\partial \Omega_1}{\partial t} \Big|_{s_0} = \frac{\partial \omega_1}{\partial s} - \sigma \Omega_1 + \Omega_2 \omega_3 - \Omega_3 \omega_2, \tag{18}$$

$$\frac{\partial \Omega_2}{\partial t} \Big|_{s_0} = \frac{\partial \omega_2}{\partial s} - \sigma \Omega_2 + \Omega_3 \omega_1 - \Omega_1 \omega_3, \tag{19}$$

$$\frac{\partial \Omega_3}{\partial t} \Big|_{s_0} = \frac{\partial \omega_3}{\partial s} - \sigma \Omega_3 + \Omega_1 \omega_2 - \Omega_2 \omega_1. \tag{20}$$

These compatibility relations show how strain changes in time due to non-uniform rotation rates (the first term in each of Eqs. (18)–(20)), growth (the second term in each of Eqs. (18)–(20)), and the geometric coupling between twisting and bending (the last two terms in each of Eqs. (18)–(20)). The compatibility relation equation (20) will

be used below to determine the dynamics of the twist strain Ω_3 . Note that Eq. (20) can be re-written in a form valid for arbitrary growth laws [41–43]:

$$\left. \frac{\partial \Omega_3}{\partial t} \right|_{s_0} = \frac{\partial \omega_3}{\partial s} - \Omega_3 \frac{\partial \mathbf{r}}{\partial s} \cdot \frac{\partial \mathbf{v}}{\partial s} + \frac{\partial \mathbf{r}}{\partial s} \times \frac{\partial^2 \mathbf{r}}{\partial s^2} \cdot \frac{\partial \mathbf{v}}{\partial s}. \quad (21)$$

2.4. Constitutive relations

The Kirchhoff constitutive relations for a rod with intrinsic twist relate the moment on a cross-section of the rod to the strain [44]:

$$\mathbf{M} = A \left(\frac{\partial \mathbf{r}}{\partial s} \times \frac{\partial^2 \mathbf{r}}{\partial s^2} \right) + C(\Omega_3 - \tau_0) \hat{\mathbf{e}}_3. \quad (22)$$

Note that $\partial \mathbf{r} / \partial s \times \partial^2 \mathbf{r} / \partial s^2 = \Omega_1 \hat{\mathbf{e}}_1 + \Omega_2 \hat{\mathbf{e}}_2$. Eq. (22) implies that in the stress-free state (defined by $\mathbf{M} = 0$), $\hat{\mathbf{e}}_1$ and $\hat{\mathbf{e}}_2$ rotate around $\hat{\mathbf{e}}_3$ with rate $\tau_0 = \hat{\mathbf{e}}_2 \cdot \partial \hat{\mathbf{e}}_1 / \partial s$, and $\hat{\mathbf{e}}_3$ is constant.

The force and moment balances for a growing rod are the same as the balances for an inextensible rod:

$$\frac{\partial \mathbf{F}}{\partial s} + \mathbf{f}_{\text{ext}} = 0, \quad (23)$$

$$\frac{\partial \mathbf{M}}{\partial s} + \hat{\mathbf{e}}_3 \times \mathbf{F} + \mathbf{m}_{\text{ext}} = 0, \quad (24)$$

where $\mathbf{F}(s, t)$ is the force the internal elastic stresses exert through the cross-section at s on the portion of the rod with arclength less than s . The external force per unit length \mathbf{f}_{ext} and moment per unit length \mathbf{m}_{ext} are measured per unit arclength. In an alternative but equivalent formulation, the elastic force and moment per unit length arise from variational derivatives of the energy:

$$E = \int ds \left(\frac{A}{2} \kappa^2 + \frac{C}{2} (\Omega - \Omega_0)^2 - \Lambda(s, t) \right), \quad (25)$$

where $\kappa^2 = |\partial^2 \mathbf{r} / \partial s^2|^2 = \Omega_1^2 + \Omega_2^2$ is the square of the curvature, and Λ the Lagrange multiplier associated with the constraint of prescribed length, $L = L_0 \exp(\sigma t)$ [41,42].

The external force per unit length \mathbf{f}_{ext} consists of a viscous drag force per unit length and an artificial short-ranged repulsive force that prevents self-crossing: $\mathbf{f}_{\text{ext}} = \mathbf{f}_{\text{visc}} + \mathbf{f}_{\text{self}}$. The external moment per unit length is purely viscous: $\mathbf{m}_{\text{ext}} = \mathbf{m}_{\text{visc}}$. The repulsive force takes the form:

$$\mathbf{f}_{\text{self}}(s, t) = \int_{|s-s'| > \delta} \frac{\beta(\mathbf{r}(s) - \mathbf{r}(s'))}{|\mathbf{r}(s) - \mathbf{r}(s')|^n} ds', \quad (26)$$

where δ is a short-distance cutoff, $n = 14$ simulates the repulsive part of a Leonard–Jones potential, and $\beta = 180$ is sufficient to keep the filament from self-crossing. The viscous force per unit length \mathbf{f}_{visc} depends on the velocity field of the ambient fluid, which in turn is coupled to the motion of the filament. For simplicity, we do not solve the full hydrodynamic problem, but instead use resistive-force theory for slender bodies [45]. Resistive-force theory amounts to the leading terms in an expansion in the aspect ratio a/L of slender-body theory, which has a nonlocal relation between force and velocity due to incompressibility. To leading order, the nonlocality can be neglected, leading to the local drag law:

$$\mathbf{f}_{\text{visc}} = -\zeta_{\perp}(\mathbf{v} - \hat{\mathbf{e}}_3 \hat{\mathbf{e}}_3 \cdot \mathbf{v}) - \zeta_{\parallel} \hat{\mathbf{e}}_3 \hat{\mathbf{e}}_3 \cdot \mathbf{v}. \quad (27)$$

Likewise, we take the viscous moment to be proportional to the tangential component of the angular velocity of the material frames:

$$\mathbf{m}_{\text{visc}} = -\zeta_{\text{R}} \hat{\mathbf{e}}_3 \hat{\mathbf{e}}_3 \cdot \boldsymbol{\omega}. \quad (28)$$

The friction coefficients in Eqs. (27) and (28) are

$$\zeta_{\perp} = \frac{4\pi\eta}{\log(L/2a) + (1/2)}, \quad \zeta_{\parallel} = \frac{2\pi\eta}{\log(L/2a) - (1/2)}, \quad \zeta_{\text{R}} = 4\pi\eta a^2, \quad (29)$$

where η is the viscosity of the ambient fluid, L the total contour length of the rod, and a the rod radius. For simplicity, we disregard the anisotropy and define $\zeta \equiv \zeta_{\perp} = \zeta_{\parallel} = 4\pi\eta/\log(L_0/2a)$, where $L_0 = L(t=0)$. Note that we have kept only the leading order terms in the logarithm of the initial aspect ratio. Thus, $\mathbf{f}_{\text{ext}} = -\zeta\mathbf{v}$. These assumptions lead to qualitative differences with the exact theory. For example, the neglect of hydrodynamic interactions implicit in the local drag approximation of Eqs. (27) and (28) will affect the time-dependence of the shape of the rod near self-contact points just before contact (see, e.g. [30]). Also, the assumption of isotropy implies that the center of mass of a deforming closed loop remains fixed [46], whereas in the exact theory the center of mass can move. These limitations of the simplified hydrodynamic theory do not prevent it from capturing the essential physics of the phenomena we wish to study, such as the onset of buckling instabilities and the subsequent evolution of complex shapes.

It is convenient for the numerical calculations of Section 3.4 to write the equations of motion in terms of position \mathbf{r} and twist strain Ω_3 . To this end, substitute the constitutive relation (22) into the moment balance equation (24) to find the force \mathbf{F} on a cross-section:

$$\mathbf{F} = -A \frac{\partial^3 \mathbf{r}}{\partial s^3} + C(\Omega_3 - \tau_0) \frac{\partial \mathbf{r}}{\partial s} \times \frac{\partial^2 \mathbf{r}}{\partial s^2} - \Lambda \frac{\partial \mathbf{r}}{\partial s}, \quad (30)$$

and the balance of the tangential components of the moment per unit length:

$$C \frac{\partial \Omega_3}{\partial s} = \zeta_{\text{R}} \omega_3. \quad (31)$$

The unknown function $\Lambda(s, t)$ occurs in Eq. (30) because the moment balance equation (24) does not determine the tangential component of \mathbf{F} . Combining Eq. (30) with the force balance equation (23) and the expressions for \mathbf{f}_{ext} yields

$$\zeta \left. \frac{\partial \mathbf{r}}{\partial t} \right|_{s_0} = -A \frac{\partial^4 \mathbf{r}}{\partial s^4} + C \frac{\partial}{\partial s} \left[(\Omega_3 - \tau_0) \frac{\partial \mathbf{r}}{\partial s} \times \frac{\partial^2 \mathbf{r}}{\partial s^2} \right] - \frac{\partial}{\partial s} \left[\Lambda \frac{\partial \mathbf{r}}{\partial s} \right] + \mathbf{f}_{\text{self}}. \quad (32)$$

Eq. (32) has the same form as the corresponding equation for the overdamped dynamics of an inextensible rod, but in Eq. (32) the s -domain (length) depends on t . To determine Λ , evaluate $\hat{\mathbf{e}}_3 \cdot \partial \mathbf{v} / \partial s = \sigma$ using Eq. (32):

$$\frac{\partial^2 \Lambda}{\partial s^2} - \frac{\partial^2 \mathbf{r}}{\partial s^2} \cdot \frac{\partial^2 \mathbf{r}}{\partial s^2} \Lambda = -A \frac{\partial \mathbf{r}}{\partial s} \cdot \frac{\partial^5 \mathbf{r}}{\partial s^5} - \zeta \sigma + \frac{\partial \mathbf{r}}{\partial s} \cdot \mathbf{f}_{\text{self}} + C(\Omega_3 - \tau_0) \frac{\partial \mathbf{r}}{\partial s} \cdot \frac{\partial^2 \mathbf{r}}{\partial s^2} \times \frac{\partial^3 \mathbf{r}}{\partial s^3}. \quad (33)$$

One can show that the function Λ in Eq. (33) is identical to the Lagrange multiplier function of Eq. (25).

To complete the determination of the dynamical equations, the torque balance (31) and compatibility relation (20) yield

$$\left. \frac{\partial \Omega_3}{\partial t} \right|_{s_0} = D \frac{\partial^2 \Omega_3}{\partial s^2} - \sigma \Omega_3 + \frac{\partial \mathbf{r}}{\partial s} \times \frac{\partial^2 \mathbf{r}}{\partial s^2} \cdot \frac{\partial \mathbf{r}}{\partial t}, \quad (34)$$

where the twist diffusion constant $D \equiv C/\zeta_{\text{R}}$. Since resistive-force theory includes the leading order terms in the expansion in a/L of the hydrodynamic drag force and torque, our equations are asymptotically consistent.

The boundary conditions which accompany Eqs. (32)–(34) depend on the situation. For a filament with free ends, the appropriate conditions are $\mathbf{M} = 0$ and $\mathbf{F} = 0$. For a closed loop, the variables \mathbf{r} , $\boldsymbol{\Omega}$, $\boldsymbol{\omega}$, \mathbf{F} , and \mathbf{M} must be periodic in s_0 with period $2\pi R_0$.

2.5. Change of basis

We close this section by returning to the claim of Section 2.2 that the spontaneous twist τ_0 does not affect the shape of an inextensible rod with circular cross-section and vanishing spontaneous curvature $\kappa_0 = 0$. Consider such a rod with $\boldsymbol{\Omega} = \tau_0 \hat{\mathbf{e}}_3$ in the stress-free state. We can eliminate τ_0 from the problem using the freedom to redefine the material frame. If

$$\hat{\mathbf{e}}'_1 = \hat{\mathbf{e}}_1 \cos \phi - \hat{\mathbf{e}}_2 \sin \phi, \quad (35)$$

$$\hat{\mathbf{e}}'_2 = \hat{\mathbf{e}}_1 \sin \phi + \hat{\mathbf{e}}_2 \cos \phi, \quad (36)$$

then

$$\Omega'_1 = \Omega_1 \cos \phi - \Omega_2 \sin \phi, \quad (37)$$

$$\Omega'_2 = -\Omega_1 \sin \phi + \Omega_2 \cos \phi, \quad (38)$$

$$\Omega'_3 = \Omega_3 + \frac{\partial \phi}{\partial s} \quad (39)$$

and

$$\omega'_1 = \omega_1 \cos \phi - \omega_2 \sin \phi, \quad (40)$$

$$\omega'_2 = -\omega_1 \sin \phi + \omega_2 \cos \phi, \quad (41)$$

$$\omega'_3 = \omega_3 + \left. \frac{\partial \phi}{\partial t} \right|_{s_0}. \quad (42)$$

Under this change of basis, $\Omega'_1 \hat{\mathbf{e}}'_1 + \Omega'_2 \hat{\mathbf{e}}'_2 = \Omega_1 \hat{\mathbf{e}}_1 + \Omega_2 \hat{\mathbf{e}}_2$ for any ϕ . Choosing $\phi = -s\tau_0$ fixes $\Omega'_3 = 0$ in the stress-free state. Thus

$$\mathbf{M} = A(\Omega'_1 \hat{\mathbf{e}}'_1 + \Omega'_2 \hat{\mathbf{e}}'_2) + C\Omega'_3 \hat{\mathbf{e}}'_3 \quad (43)$$

the parameter τ_0 has been eliminated from the constitutive relation. Note that our argument up to this point holds for a growing rod as well.

Now consider the effect of the transformation (35) and (36) on the compatibility relations. Once again, even in the presence of exponential growth, the compatibility equations take the same form, e.g.:

$$\left. \frac{\partial \Omega'_3}{\partial t} \right|_{s_0} = \frac{\partial \omega'_3}{\partial s} - \sigma \Omega'_3 + \Omega'_1 \omega'_2 - \Omega'_2 \omega'_1. \quad (44)$$

For an inextensible rod, $\omega'_3 = \omega_3$, since $s = s_0$ if $\sigma = 0$. Therefore, the change of basis (35) and (36) does not affect the rotational drag or translational drag equations, and we conclude that τ_0 is not a physical parameter for an inextensible rod with circular cross-section and no spontaneous curvature. However, we expect the opposite conclusion for a growing rod, since we saw in Section 2.2 that τ_0 has physical meaning. In fact, once τ_0 is eliminated

from the constitutive relation using Eqs. (35) and (36), a new τ_0 -dependent term appears in the torque balance equation (31):

$$C \frac{\partial \Omega_3'}{\partial s} = \zeta_R (\omega_3' + \sigma s \tau_0). \quad (45)$$

Therefore, τ_0 cannot be eliminated from the equations of motion for this mode of growth.

3. The growing elastic loop

In this section we treat the problem of a growing elastic loop with preferred twist τ_0 . As described in Section 1, this example is motivated by the growth of *B. subtilis* filaments from a spore. Sometimes the ends of the growing filament stick to the spore coat, leading to a closed loop [18]. The filament lengthens, depleting the twist, but the closed geometry prevents the rotation of cross-sections normally seen in unconstrained filaments. Thus, twist stress builds up, and the filament eventually writhes and coils. Although the model does not address the writhing and coiling of unconstrained filaments, it displays some of the features exhibited by *B. subtilis* loops.

3.1. Buckling and writhing instabilities

To study the stability of an exponentially growing circular loop with preferred twist τ_0 , we begin with the unperturbed solution. The unperturbed loop lies in the $z = 0$ plane and has radius $R = R_0 \exp(\sigma t)$. Since each material point on the filament moves radially outward with fixed z in unperturbed growth, the angular velocity vanishes, $\omega^{(0)} = 0$, where we use the superscript, (0), to denote the unperturbed value. The bending part of the energy (25) decreases exponentially as the loop grows because $\kappa^{(0)} = 1/R$. However, the twist energy density *increases* because the closed geometry prevents the cross-sections from rotating with the rate $\sigma s \tau_0$ required to attain the twist state of zero energy. If we assume for simplicity that $\Omega_3^{(0)}(s, t = 0) = \tau_0$, then the exponentially increasing length leads to an exponentially decreasing twist density, $\Omega_3^{(0)}(s, t) = \tau_0 \exp(-\sigma t)$. To summarize, the moment on a cross-section takes the form:

$$\mathbf{M}^{(0)} = \frac{A}{R_0} e^{-\sigma t} \hat{\mathbf{z}} + C \tau_0 (e^{-\sigma t} - 1) \hat{\boldsymbol{\phi}}. \quad (46)$$

Note that it is much more convenient to express \mathbf{M} in terms of the cylindrical coordinate unit vectors $\{\hat{\mathbf{z}}, \hat{\boldsymbol{\rho}}, \hat{\boldsymbol{\phi}}\}$ instead of the material frame vectors $\{\hat{\mathbf{e}}_1^{(0)}, \hat{\mathbf{e}}_2^{(0)}, \hat{\mathbf{e}}_3^{(0)}\}$, since $\hat{\mathbf{e}}_1^{(0)}$ and $\hat{\mathbf{e}}_2^{(0)}$ continuously rotate about $\hat{\mathbf{e}}_3^{(0)}$ as s increases. A choice of frame which does not rotate about the tangent vector as arclength increases is a *natural* frame [47]. We will use the natural frame extensively in the linear stability analysis of Section 3.3.

Since the filament is simultaneously bent and twisted, moment balance (24) implies a component of force in the z -direction, whereas force balance (23) leads to a tangential component proportional to the growth rate σ :

$$\mathbf{F}^{(0)} = -\zeta \sigma R^2 \hat{\boldsymbol{\phi}} + \frac{C \tau_0}{R} (e^{-\sigma t} - 1) \hat{\mathbf{z}}. \quad (47)$$

The tangential force on the cross-section is compressive and grows exponentially in time, eventually leading to an Euler-like buckling instability when $\zeta \sigma R^2 \approx A/R^2$, or $R = R_1 \approx [A/\zeta \sigma]^{1/4}$ (cf. [29–31]). The Euler buckling time scales as $t_E \approx \sigma^{-1} \log[A/\zeta \sigma R_0^4]$ (when $A/\zeta \sigma R_0^4 < 1$, the loop begins to buckle at $t = 0$). In Section 3.3, we will refine this estimate using our linear stability calculation and see that the appropriate buckling time at small σ actually scales as σ^{-2} , since in this regime, a growing perturbation does not become noticeable until long after the perturbation begins to grow. However, our numerical calculations of Section 3.4 reveal that the correct picture is even

more complicated: for sufficiently small $\tau_0 R_0$, a secondary instability arises and grows before the linear instability has significant amplitude. In addition to the Euler buckling, there is also a writhing instability. The magnitude of the twist moment increases as $|C\tau_0(1 - \exp(-\sigma t))|$ as the filament lengthens, leading to a writhing instability (like that of a twisted ring [48–50]) when $C\tau_0(1 - \exp(-\sigma t)) \approx A/2\pi R$, or $t_W \approx \sigma^{-1} \log[1 + 1/\tau_0 R_0]$ (assuming $A \approx C$). Note that the critical time for writhing is $t_W \approx \sigma^{-1} \log[1/R_0\tau_0]$ for $R_0\tau_0 \ll 1$, and $t_W \approx 1/\sigma R_0\tau_0$ for $R_0\tau_0 \gg 1$. The sense of rotation of the cross-sections of unconstrained filaments determines the handedness of the coils that form after the instability of the ring: positive τ_0 (counter-clockwise rotation when viewed from the direction of increasing s) leads to right-handed plectonemic braids. Note that drag is the ultimate cause for the Euler buckling instability; once growth ceases, the buckled filament relaxes back to the unperturbed circular shape. Since the writhing instability arises not from drag but instead from the frustration of growth-induced twist stress, the braided post-instability shape remains after growth ceases. For small enough $\tau_0 R_0$, we will see in Section 3.4 that the small intrinsic twist biases the Euler buckling, leading to solenoidal shapes, which relax to plectonemes if growth halts after a sufficiently long time. Observations of the growing fibers suggest that writhing is the dominant mechanism in the instability of a closed loop [18]. Using $A = 10^{-12}$ erg cm [28], $\sigma = 2 \times 10^{-4}$ s $^{-1}$, $L = 10^{-3}$ cm, $a = 3 \times 10^{-5}$ cm, and $\zeta = \zeta_{\perp} \approx 10^{-1}$ erg s/cm 3 (see Eq. (29)) leads to $[A/\zeta\sigma]^{1/4} \approx 150$ μ m, which is much larger than the observed critical radius and implies that growth-induced Euler buckling is not important. Thus, we can use the critical radius of the twisted ring to estimate τ_0 ; assuming τ_0 is comparable to or smaller than $1/R_0$, where R_0 is the initial radius, and using $R_2 \approx 2 \times 10^{-4}$ cm as the experimentally observed critical radius [18], we find $\tau_0 \approx 10^4$ cm $^{-1}$. This twist rate corresponds to a few turns per cell. It is intriguing to note that the corresponding length scale is close to the pitch of helical filaments of mbl, a recently discovered protein which resides near the cell wall and plays a role in maintaining the shape of *B. subtilis* cells [51].

3.2. The natural frame

Before studying the evolution of small perturbations of the growing circular shape, we consider the choice of representation. Since only the shape and twist are of interest, it is convenient to use an intrinsic representation, such as the material frame. However, we saw in the solution of the unperturbed problem of Section 3.1 that the natural frame leads to further simplification. The advantages of the natural frame over the material frame are even greater for the linear stability analysis, and more generally for the full nonlinear problem [42,52].

In a natural orthonormal frame $\{\hat{\mathbf{n}}_1, \hat{\mathbf{n}}_2, \hat{\mathbf{e}}_3\}$ the instantaneous rate of rotation of $\hat{\mathbf{n}}_1$ about $\hat{\mathbf{e}}_3$ is zero [42,47,52]:

$$\hat{\mathbf{n}}_1 \cdot \frac{\partial \hat{\mathbf{n}}_2}{\partial s} = 0. \quad (48)$$

A rotation of $\{\hat{\mathbf{n}}_1, \hat{\mathbf{n}}_2\}$ about $\hat{\mathbf{e}}_3$ by uniform (arclength-independent) angle leaves the condition (48) invariant; every space curve has a family of natural frames, the members of which are related to each other by rotation through a uniform angle. To construct a natural frame from the material frame $\{\hat{\mathbf{e}}_1, \hat{\mathbf{e}}_2, \hat{\mathbf{e}}_3\}$, rotate the material frame at s by minus the accumulated rotation angle $\vartheta = \int_0^s ds' \Omega_3$:

$$\hat{\mathbf{n}}_1 = \cos \vartheta \hat{\mathbf{e}}_1 - \sin \vartheta \hat{\mathbf{e}}_2, \quad (49)$$

$$\hat{\mathbf{n}}_2 = \sin \vartheta \hat{\mathbf{e}}_1 + \cos \vartheta \hat{\mathbf{e}}_2. \quad (50)$$

The natural frame is nonlocal in the sense that deformations of the filament centerline in the region $s' < s$ affect the natural frame at s .

Our formulas can be further simplified with complex notation. For example, if $\boldsymbol{\epsilon} \equiv \hat{\mathbf{n}}_1 + i\hat{\mathbf{n}}_2$, then Eqs. (49) and (50) become

$$\boldsymbol{\epsilon} = (\hat{\mathbf{e}}_1 + i\hat{\mathbf{e}}_2) e^{i\vartheta}. \quad (51)$$

The vector $\boldsymbol{\epsilon}$ is a complex normal vector. Note that $\boldsymbol{\epsilon} \cdot \boldsymbol{\epsilon} = 0$; therefore, $\boldsymbol{\epsilon} \cdot \partial\boldsymbol{\epsilon}/\partial s = 0$. Furthermore, the defining property $\hat{\mathbf{n}}_1 \cdot \partial\hat{\mathbf{n}}_2/\partial s = 0$ implies $\boldsymbol{\epsilon}^* \cdot \partial\boldsymbol{\epsilon}/\partial s = 0$. Thus, $\partial\boldsymbol{\epsilon}/\partial s$ is proportional to $\hat{\mathbf{e}}_3$. In analogy with the Frenet–Serret equation $\partial\hat{\mathbf{n}}/\partial s = -\kappa\hat{\mathbf{t}}$, we define the complex curvature Ψ via

$$\frac{\partial\boldsymbol{\epsilon}}{\partial s} = -\Psi\hat{\mathbf{e}}_3, \quad (52)$$

where

$$\Psi = -\hat{\mathbf{e}}_3 \cdot \frac{\partial\boldsymbol{\epsilon}}{\partial s} = \boldsymbol{\epsilon} \cdot \frac{\partial\hat{\mathbf{e}}_3}{\partial s}, \quad (53)$$

$$\Psi = (-i\Omega_1 + \Omega_2) e^{i\vartheta}. \quad (54)$$

Also, the rate of change along s of the unit tangent vector is the complex curvature times the complex normal vectors:

$$\frac{\partial\hat{\mathbf{e}}_3}{\partial s} = \frac{1}{2}(\Psi\boldsymbol{\epsilon}^* + \Psi^*\boldsymbol{\epsilon}). \quad (55)$$

Note that rotation of a natural frame about $\hat{\mathbf{e}}_3$ by a uniform angle leads to a constant shift in the phase of Ψ . For example, the natural frame arising from the construction (49) and (50) applied to the Frenet–Serret normal and binormal has

$$\boldsymbol{\epsilon} = (\hat{\mathbf{n}} + i\hat{\mathbf{b}}) \exp\left(i \int \tau ds\right), \quad (56)$$

since torsion is the rate at which $\hat{\mathbf{n}}$ and $\hat{\mathbf{b}}$ twist around the tangent vector. The corresponding complex curvature is

$$\Psi_{\text{FS}} = \kappa \exp\left(i \int \tau ds\right); \quad (57)$$

the ratio of Ψ and Ψ_{FS} is a constant phase.

To complete the specification of the kinematics of the natural frame, we introduce the complex angular velocity describing the rate of change with time of the unit tangent vector:

$$\Pi \equiv \boldsymbol{\epsilon} \cdot \frac{\partial\hat{\mathbf{e}}_3}{\partial t}, \quad (58)$$

$$\Pi = (-i\omega_1 + \omega_2) e^{i\vartheta}. \quad (59)$$

In terms of the natural frame variables, the compatibility relations (18)–(20) become

$$\left. \frac{\partial\Psi}{\partial t} \right|_{s_0} = \frac{\partial\Pi}{\partial s} - \sigma\Psi - i\Psi\omega_3(0) + i\Psi \int_0^s ds' \text{Im}(\Psi^*\Pi), \quad (60)$$

$$\left. \frac{\partial\Omega_3}{\partial t} \right|_{s_0} = \frac{\partial\omega_3}{\partial s} - \sigma\Omega_3 + \text{Im}(\Psi^*\Pi). \quad (61)$$

The integral in Eq. (60) reflects the nonlocality of the natural frame, and arises from the temporal rate of change of ϑ :

$$\left. \frac{\partial\vartheta}{\partial t} \right|_{s_0} = \left. \frac{\partial}{\partial t} \right|_{s_0} \int_0^{s_0} e^{\sigma t'} \Omega_3(s', t) ds', \quad (62)$$

$$\left. \frac{\partial \vartheta}{\partial t} \right|_{s_0} = \left. \frac{\partial}{\partial t} \right|_{s_0} \int_0^{s_0} \Omega_3(s'_0 e^{\sigma t}, t) e^{\sigma t} ds'_0, \quad (63)$$

$$\left. \frac{\partial \vartheta}{\partial t} \right|_{s_0} = \int_0^s \left[\frac{\partial \Omega_3}{\partial t} + \sigma \Omega_3 \right] ds'. \quad (64)$$

Eq. (60) follows from Eqs. (64), (18)–(20), and the identity $\Omega_1 \omega_2 - \Omega_2 \omega_1 = \text{Im}(\Psi^* \Pi)$.

In the natural frame variables, the moment \mathbf{M} obeys

$$\mathbf{M} = A \frac{1}{2} i (\Psi \boldsymbol{\epsilon}^* - \Psi^* \boldsymbol{\epsilon}) + C(\Omega_3 - \tau_0) \hat{\mathbf{e}}_3. \quad (65)$$

Just as in Section 2.4, moment balance (24) determines the perpendicular component of the force on a cross-section:

$$\mathbf{F} = F_{\parallel} \hat{\mathbf{e}}_3 + \frac{1}{2} (\boldsymbol{\epsilon}^* F_{\perp} + \boldsymbol{\epsilon} F_{\perp}^*), \quad (66)$$

$$F_{\perp} = -A \frac{\partial \Psi}{\partial s} + i C \Psi (\Omega_3 - \tau_0). \quad (67)$$

Recall that F_{\parallel} is not determined by moment balance since only the perpendicular components of \mathbf{F} enter Eq. (24); F_{\parallel} is determined by the condition $\hat{\mathbf{e}}_3 \cdot \partial \mathbf{v} / \partial s = \sigma$.

Defining the tangential and perpendicular components f_{\parallel} and f_{\perp} of the force per unit length:

$$\frac{\partial \mathbf{F}}{\partial s} = \hat{\mathbf{e}}_3 f_{\parallel} + \frac{1}{2} (\boldsymbol{\epsilon}^* f_{\perp} + \boldsymbol{\epsilon} f_{\perp}^*), \quad (68)$$

it follows from Eqs. (52), (55), (66) and (67) that

$$f_{\parallel} = \frac{\partial F_{\parallel}}{\partial s} + \frac{A}{2} (\Psi \Psi_s^* + \Psi_s \Psi^*) \quad (69)$$

and

$$f_{\perp} = F_{\perp} \Psi - A \frac{\partial^2 \Psi}{\partial s^2} + i C \frac{\partial}{\partial s} [\Psi (\Omega_3 - \tau_0)]. \quad (70)$$

Note $f_{\parallel} = \partial(F_{\parallel} + A|\Psi|^2/2)/\partial s = -\partial \Lambda / \partial s$; in terms of f_{\parallel} and f_{\perp} the condition $\hat{\mathbf{e}}_3 \cdot \partial \mathbf{v} / \partial s = \sigma$ becomes

$$\zeta \sigma = \frac{\partial f_{\parallel}}{\partial s} - \frac{1}{2} f_{\perp} \Psi^* - \frac{1}{2} f_{\perp}^* \Psi. \quad (71)$$

Finally, the force per unit length determines the complex angular velocity through the relations $\zeta \mathbf{v} = \partial \mathbf{F} / \partial s$ and $\boldsymbol{\epsilon} \cdot \partial \mathbf{v} / \partial s = \Pi$, or

$$\zeta \Pi = \frac{\partial f_{\perp}}{\partial s} + \Psi f_{\parallel}. \quad (72)$$

Likewise, the tangential component of the angular velocity is given by Eq. (31). In summary, the equations of motion for the filament in the natural frame are Eqs. (60) and (61), (69)–(72), and (31).

3.3. Linear stability analysis

We now return to the stability analysis of a growing circular ring. We write the shape as $\mathbf{r} = (R + r^{(1)}) \hat{\boldsymbol{\rho}} + z^{(1)} \hat{\mathbf{z}}$ and work to first order in $r^{(1)}$ and $z^{(1)}$. It is convenient to find the equations of motion for $\Psi^{(1)}$ and $\Omega_3^{(1)}$ first, and then

express these equations in terms of $r^{(1)}$ and $z^{(1)}$. To this end, we choose $\{\hat{\mathbf{n}}_1^{(0)}, \hat{\mathbf{n}}_2^{(0)}\} = \{-\hat{\boldsymbol{\rho}}, \hat{\mathbf{z}}\}$ to make $\Psi^{(0)} = 1/R$. Expanding (57) to first order leads to

$$\Psi = \kappa^{(0)} + \kappa^{(1)} + i\kappa^{(0)} \int \tau^{(1)} ds, \quad (73)$$

since the unperturbed loop has zero torsion, $\tau^{(0)} = 0$. To express κ and τ in terms of $r^{(1)}$ and $z^{(1)}$, use the Frenet–Serret equations (8) and (9) and $s = R\phi$ (to leading order) to find

$$\kappa \approx \frac{1}{R} - \frac{1}{R^2}(r^{(1)} + r_{\phi\phi}^{(1)}) \quad (74)$$

and

$$\tau \approx \tau^{(1)} = \frac{1}{R^2}(z_{\phi}^{(1)} + z_{\phi\phi\phi}^{(1)}). \quad (75)$$

Thus, $\Psi = 1/R + \xi + i\eta$, with

$$\xi = -\frac{1}{R^2}(r^{(1)} + r_{\phi\phi}^{(1)}), \quad (76)$$

$$\eta = \frac{1}{R^2}(z^{(1)} + z_{\phi\phi}^{(1)}). \quad (77)$$

As described in Section 3.1, the unperturbed angular velocities vanish: $\Pi^{(0)} = 0$, $\omega_3^{(0)} = 0$; furthermore, Eq. (47) together with (69) and (70) imply $f_{\perp}^{(0)} = F_{\parallel}^{(0)}/R = -\zeta\sigma R$ and $f_{\parallel}^{(0)} = 0$. Expanding the equations of motion to first order, we find

$$\left. \frac{\partial \Psi^{(1)}}{\partial t} \right|_{s_0} = \frac{\partial \Pi^{(1)}}{\partial s} - \sigma \Psi^{(1)} - i\Psi^{(0)}\omega_3^{(1)}(0) + i\Psi^{(0)} \int_0^s ds' \text{Im}(\Psi^{(0)*} \Pi^{(1)}), \quad (78)$$

$$\left. \frac{\partial \Omega_3^{(1)}}{\partial t} \right|_{s_0} = D \frac{\partial^2 \Omega_3^{(1)}}{\partial s^2} - \sigma \Omega_3^{(1)} + \text{Im}(\Psi^{(0)*} \Pi^{(1)}), \quad (79)$$

$$0 = \frac{\partial f_{\parallel}^{(1)}}{\partial s} - \text{Re}(f_{\perp}^{(0)} \Psi^{(1)*}) - \text{Re}(f_{\perp}^{(1)} \Psi^{(0)*}), \quad (80)$$

$$\zeta \Pi^{(1)} = \frac{\partial f_{\perp}^{(1)}}{\partial s} + \Psi^{(0)} f_{\parallel}^{(1)}, \quad (81)$$

where $f_{\parallel}^{(1)}$ and $f_{\perp}^{(1)}$ are determined by expanding (69) and (70) to first order. Inspection of (78)–(81) and (69) and (70) reveals that $r^{(1)} = \hat{r}^{(1)} \cos(n\phi)$, $z^{(1)} = \hat{z}^{(1)} \sin(n\phi)$, $F_{\parallel}^{(1)} = \hat{F}_{\parallel} \cos(n\phi)$, and $\Omega_3^{(1)} = \hat{\Omega}_3 \cos(n\phi)$, with n a positive integer. This choice of origin for s and Eq. (31) imply $\hat{\omega}_3^{(1)}(0) = 0$. The perturbation $\hat{r}^{(1)} \cos \phi$ corresponds to a translation of the ring in the $z = 0$ plane; likewise, the perturbation $\hat{z}^{(1)} \sin \phi$ corresponds to a rotation of the ring about an axis in the $z = 0$ plane. Thus, the $n = 1$ perturbations are rigid motions, leading to no change in curvature: $\xi = \eta = 0$ (see Eqs. (76) and (77)). Inserting the perturbations into (78), (79) and (81) and using (80) to eliminate \hat{F}_{\parallel} yields a linear system of differential equations for $\hat{r}^{(1)}$, $\hat{z}^{(1)}$, and $\hat{\Omega}_3$:

$$\hat{r}_t^{(1)} = \left[\sigma \frac{n^4 + 3}{n^2 + 1} - \frac{A}{\zeta R^4} \frac{n^2(n^2 - 1)^2}{n^2 + 1} \right] \hat{r}^{(1)} - \frac{C}{\zeta R^3} (\Omega_3^{(0)} - \tau_0) \frac{n^3(n^2 - 1)}{n^2 + 1} \hat{z}^{(1)}, \quad (82)$$

$$\hat{z}_t^{(1)} = -\frac{C}{\zeta R^3}(\Omega_3^{(0)} - \tau_0)n(n^2 - 1)\hat{r}^{(1)} + \left[\sigma n^2 - \frac{A}{\zeta R^4}n^2(n^2 - 1) \right] \hat{z}^{(1)} - \frac{C}{\zeta R^2}n\hat{\Omega}_3, \quad (83)$$

$$\hat{\Omega}_{3t} = \frac{C}{\zeta R^3}(\Omega_3^{(0)} - \tau_0)n^2(1 - n^2)\frac{\hat{r}^{(1)}}{R^2} + \left[\frac{An^2}{\zeta R^4} - \sigma \right] n(1 - n^2)\frac{\hat{z}^{(1)}}{R^2} - \left[\sigma + \frac{Dn^2}{R^2} + \frac{Cn^2}{\zeta R^4} \right] \hat{\Omega}_3. \quad (84)$$

Eqs. (82) and (83) hold for $n \neq 1$, and Eq. (84) holds for all integer $n \geq 1$. For $n = 1$, the shape drops out of Eq. (84) since the $n = 1$ shape perturbations are rigid motions. Note that τ_0 enters (82)–(84) in the combination $\Omega_3^{(0)} - \tau_0 = \tau_0(\exp(-\sigma t) - 1)$; τ_0 drops out of the equations when $\sigma = 0$, in accord with the general arguments of Section 2.5.

We can simplify the linear system (82)–(84) by exploiting the large ratio of relaxation time scales for twisting and bending modes:

$$t_{\text{bend}} \gg t_{\text{twist}} \quad (85)$$

for $R \approx 10 \mu\text{m}$ and the *B. subtilis* parameters of Section 3.1, $t_{\text{bend}} \equiv \zeta R^4/A \approx 10^{-1} \text{ s}$ and $t_{\text{twist}} \equiv R^2/D = \zeta_R R^2/C \approx 10^{-4} \text{ s}$. As time passes and the filament lengthens, t_{bend} and t_{twist} increase exponentially, but $t_{\text{bend}} \gg t_{\text{twist}}$ for all time. Therefore, twist perturbations $\hat{\Omega}$ relax immediately, and (82)–(84) may be simplified by setting $\hat{\Omega}$ to zero. Using the initial radius for the bending relaxation time ($t_{\text{bend}} = \zeta R_0^4/A$) and assuming $C/A = 1$ for simplicity, (82) and (83) reduce to

$$\dot{\mathbf{q}} = \mathbf{L}\mathbf{q}, \quad (86)$$

where

$$\mathbf{q} = \begin{pmatrix} \hat{r}^{(1)} \\ \hat{z}^{(1)} \end{pmatrix} \quad (87)$$

and

$$\mathbf{L} = \begin{bmatrix} \sigma \frac{n^4 + 3}{n^2 + 1} - \frac{e^{-4\sigma t}}{t_{\text{bend}}} \frac{n^2(n^2 - 1)^2}{n^2 + 1} & -\frac{\tau_0 R_0 e^{-3\sigma t}}{t_{\text{bend}}} (e^{-\sigma t} - 1) \frac{n^3(n^2 - 1)}{n^2 + 1} \\ -\frac{\tau_0 R_0 e^{-3\sigma t}}{t_{\text{bend}}} (e^{-\sigma t} - 1)n(n^2 - 1) & \sigma n^2 - \frac{e^{-4\sigma t}}{t_{\text{bend}}} n^2(n^2 - 1) \end{bmatrix}. \quad (88)$$

Since \mathbf{L} depends on time, the system (86) is nonautonomous, and classical modal analysis [53] does not apply. Note also that \mathbf{L} is not a normal operator: $[\mathbf{L}, \mathbf{L}^T] \neq 0$. Therefore, the eigenvectors of \mathbf{L} are not perpendicular, which in general signals the possibility of transient or algebraic growth of perturbations [54]. However, \mathbf{L} is only weakly non-normal, since the eigenvectors are almost perpendicular. A similar conclusion applies to the problem of a ring with twist but no growth ($\sigma = 0$) in a viscous fluid (cf. [43,50]). Therefore, we do not expect the phenomenon of transient growth of perturbations in our problem. Nevertheless, the methods developed to study non-normal linear problems are well suited to nonautonomous problems such as (86) [55].

We will characterize the growth of perturbations by the amplification of the magnitude of $\mathbf{q}(0)$. The optimal amplification $G(t)$ is defined by maximizing this factor over all initial conditions:

$$G(t) \equiv \max_{\mathbf{q}(0)} \frac{\mathbf{q}(t) \cdot \mathbf{q}(t)}{\mathbf{q}(0) \cdot \mathbf{q}(0)}. \quad (89)$$

(A more physical choice for the optimal growth rate would be to use the bending energy to second order in $\hat{r}^{(1)}$ and $\hat{z}^{(1)}$ instead of $\mathbf{q} \cdot \mathbf{q}$; it turns out that either choice yields essentially the same $G(t)$.) To compute $G(t)$, recast

Eq. (86) as an equation for the propagator matrix \mathbf{B} :

$$\dot{\mathbf{B}} = \mathbf{L}\mathbf{B}, \quad (90)$$

where $\mathbf{B}(0) = \mathbf{I}$ and $\mathbf{q}(t) = \mathbf{B}(t)\mathbf{q}(0)$. Thus, the optimal growth factor is the Rayleigh quotient:

$$G(t) = \max_{\mathbf{q}(0)} \frac{\mathbf{q}(0) \cdot \mathbf{B}^T(t)\mathbf{B}(t)\mathbf{q}(0)}{\mathbf{q}(0) \cdot \mathbf{q}(0)}, \quad (91)$$

or $G(t) = \lambda_+$, where λ_+ is the largest eigenvalue of $\mathbf{B}^T(t)\mathbf{B}(t)$ [56]. When \mathbf{L} is a t -independent normal matrix, then $\lambda_+ = \exp(2\Lambda_+t)$, where Λ_+ is the largest eigenvalue of \mathbf{L} . Note that since $G(t)$ is maximized at each t over all initial conditions $\mathbf{q}(0)$, the maximum amplitudes at two different times may correspond to two different initial conditions $\mathbf{q}(0)$. We computed $G(t)$ by using standard Runge–Kutta techniques to solve for $\mathbf{B}(t)$ [57].

Inspection of the diagonal components of \mathbf{L} (88) reveals that for sufficiently rapid growth, $\sigma > \sigma_c \equiv n^2(n^2 - 1)^2 / [(n^2 + 3)t_{\text{bend}}]$, the loop deforms away from its circular shape as soon as it begins to grow. When the rate of growth of the ring is sufficiently slow, $\sigma < \sigma_c$, bending stiffness stabilizes the circular shape for $\sigma t \ll 1$ and perturbations decay roughly as $\exp(-n^4 t / t_{\text{bend}})$. Thus, the growth factor G decays extremely rapidly with increasing n at early times. As time passes, the loop lengthens and eventually buckles, with the nature of the buckling dependent on the magnitude of τ_0 . For $\tau_0 R_0 \ll 1$, the distortion is the three-dimensional analog of the in-plane Euler buckling studied by Shelley and Ueda [29,30] and Drasdo [31]. For $\tau_0 R_0 \gg 1$, the off-diagonal elements of \mathbf{L} are large [see (88)], writhing dominates the nature of the initial distortion, and $G(t)$ increases roughly as $\exp(2\tau_0 R_0 n^3 t / t_{\text{bend}})$ in the intermediate regime $\sigma t \approx 1$. In the late-time regime $\sigma t \gg 1$, $G(t) \propto \exp(2n^2 \sigma t)$ for any value of $\tau_0 R_0$ or t_b . These results are summarized in Fig. 5.

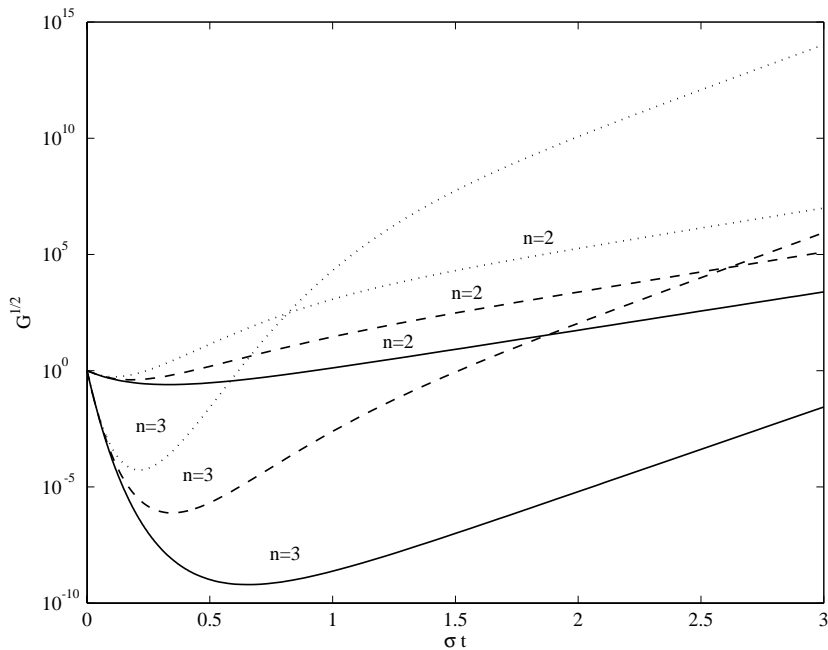


Fig. 5. Optimal growth factors for $\sigma t_{\text{bend}} = 0.5 (< \sigma_c t_{\text{bend}})$. Solid line: $R_0 \tau_0 = 0$; dashed line: $R_0 \tau_0 = 5$; dotted line: $R_0 \tau_0 = 10$. Note that the intermediate regime of rapid growth of $G(t)$ is most apparent for $R_0 \tau_0 = 10$, especially for $n = 3$.

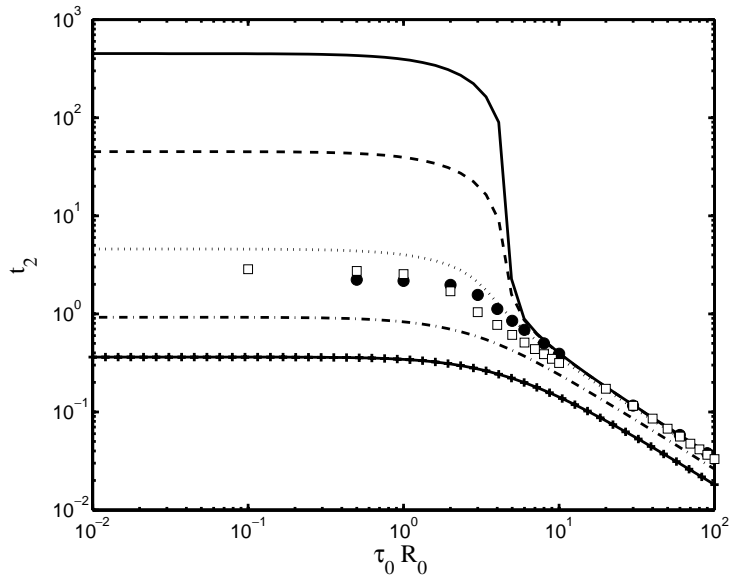


Fig. 6. Time t_2 for optimal perturbation to regain initial amplitude as a function of $R_0 \tau_0$ for $\sigma t_{\text{bend}} = 0.001$ (solid line), $\sigma t_{\text{bend}} = 0.01$ (dashed line), $\sigma t_{\text{bend}} = 0.1$ (dotted line), $\sigma t_{\text{bend}} = 0.5$ (dashed-dotted line), and $\sigma t_{\text{bend}} = 1$ (solid line with small dots). The large filled dots are the results of numerical simulations of the full nonlinear equations with $\sigma t_{\text{bend}} = 0.01$ and the open squares are with $\sigma t_{\text{bend}} = 0.1$; see Section 3.4.

There are two different times which may be chosen to represent the time of the instability. The estimate for the buckling time of Section 3.1 amounts to the time t_1 at which $G(t)$ reaches its minimum value and starts to increase. However, since the rate of decay of $G(t)$ in the stable period can be very different from the rate of growth of $G(t)$ in the unstable period, the time at which a perturbation becomes noticeable may be significantly greater than t_1 . Thus, it is natural to define the time for the onset of the instability to be the time t_2 at which the amplitude of the optimal perturbation regains its initial value: $G(t_2) = 1$. The graphs of Fig. 5 suggest that t_2 and t_1 are comparable whenever $R_0 \tau_0$ is large enough for the intermediate growth regime of rapid growth discussed above to be present. However, if $R_0 \tau_0$ is small enough that this intermediate regime is absent, then t_2 will be much greater than t_1 when the extensional growth rate is slow, $\sigma t_{\text{bend}} \ll 1$. Fig. 6 shows how dramatic this difference can be. For $R_0 \tau_0 \ll 1$ and $\sigma t_{\text{bend}} \ll 1$:

$$t_2 \approx \frac{1}{\sigma^2 t_{\text{bend}}} \frac{n^2(n^2 - 1)^2}{4(n^4 + 3)}, \tag{92}$$

whereas $t_1 \propto 1/\sigma$. When $R_0 \tau_0 \gg 1$, both t_1 and t_2 scale as $1/\sigma$ (see Fig. 6). Thus, for small σt_{bend} , there is a sharp transition in the onset time t_2 as a function of $R_0 \tau_0$. In Section 3.4 we will see how this prediction of the linear theory captures the early time dynamics for $R_0 \tau_0 \gg 1$, but that nonlinearities intervene before $t = t_2$ for $R_0 \tau_0 \ll 1$.

The curves for the onset time t_2 of Fig. 6 were computed from the linearized equation (86) using the adiabatic theorem. If $\sigma t_{\text{bend}} \ll 1$, and if \mathbf{L} were normal, then the adiabatic theorem [58] would imply that

$$\mathbf{B} \approx \mathbf{v}_+ \mathbf{v}_+ \exp\left(2 \int_0^t \Lambda_+(t') dt'\right) + \mathbf{v}_- \mathbf{v}_- \exp\left(2 \int_0^t \Lambda_-(t') dt'\right), \tag{93}$$

where $\mathbf{v}_\pm \mathbf{v}_\pm$ are the dyads formed from the eigenvectors $\mathbf{v}_\pm(t)$ of $\mathbf{L}(t)$. Since \mathbf{L} is not normal, Eq. (93) is in error by an amount governed by $\mathbf{v}_+ \cdot \mathbf{v}_-$, which is never more than about 0.1 and is often much smaller. Note also that if

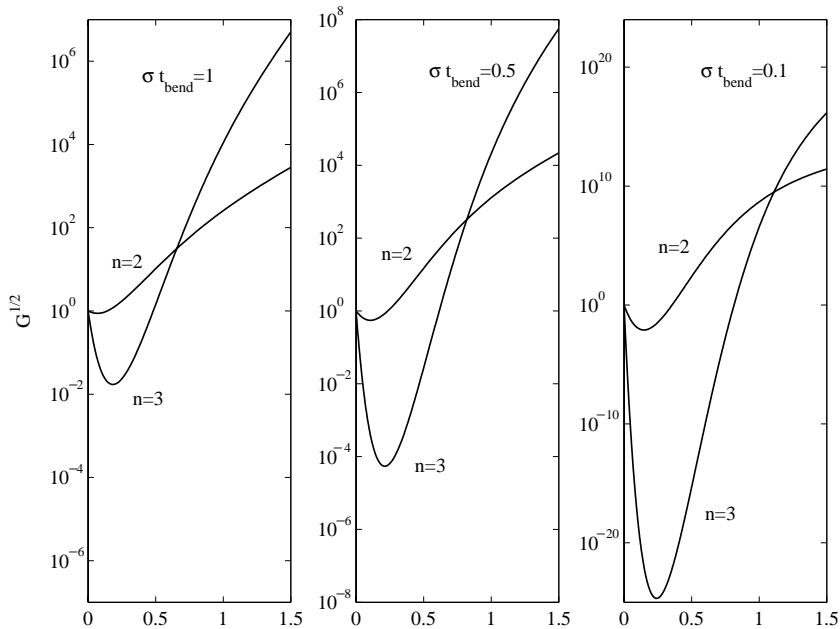


Fig. 7. Optimal growth factors for $\tau_0 R_0 = 10$ and $\sigma t_{\text{bend}} = 1.0, 0.5, 0.1$.

$\sigma t_{\text{bend}} \gg 1$, then the off-diagonal elements of \mathbf{L} are small compared to the diagonal elements, causing the equations for $\hat{r}^{(1)}$ and $\hat{z}^{(1)}$ to decouple and leading to

$$G(t) \approx \exp\left(2 \int_0^t \Lambda_+(t') dt'\right), \tag{94}$$

where $\Lambda_+(t)$ is the largest eigenvalue of $\mathbf{L}(t)$. Thus, in both extremes $\sigma t_{\text{bend}} \gg 1$ and $\sigma t_{\text{bend}} \ll 1$, $G(t) \approx \exp(2 \int \Lambda_+ dt')$. This result is especially useful in the limit of small growth rate $\sigma t_{\text{bend}} \ll 1$, since the rapid relaxation and growth of bending modes makes it difficult to solve for \mathbf{B} numerically.

Fig. 7 shows the optimal growth factors for the first two modes ($n = 2$ and 3) for $\sigma t_{\text{bend}} = 1.0, 0.5, 0.1$ and $R_0 \tau_0 = 10$. For both the intermediate writhing regime and the large- σt asymptotic regime, the rate of increase of the growth factor increases with mode number n . As σt_{bend} increases, the time at which the growth factor for the $n = 3$ mode overtakes that of the $n = 2$ mode decreases because the instability of each mode occurs at earlier times. For the larger values of σt_{bend} , the $n = 3$ mode overtakes the $n = 2$ mode before the amplitudes have grown large enough for nonlinearities to come into play. Thus, we expect to see double-stranded plectonemic braids with two hairpin turns for small σt_{bend} , and braids with three or more hairpin turns when σt_{bend} is large. The numerical computations of Section 3.4 confirm these expectations.

3.4. Numerical solution of the nonlinear equations

We solved the closed set of Eqs. (32)–(34) using a pseudospectral method [59] for the backbone dynamics (32), direct integration of (33) at each time step using finite differences to find Λ , and a Crank–Nicholson routine for the twist dynamics (34). We used initial conditions such that the backbone of the loop is perturbed from circular shape with $R_0 = 1$ by a few small-amplitude modes ($n = 2$ – 5). Depending on the simulation, Ω_3 ranged from somewhat less than τ_0 to τ_0 . Fig. 8 shows a time series of the shape of the growing loop with $\tau_0 R_0 = 10$, $\Omega_3(t = 0) = \tau_0$, and

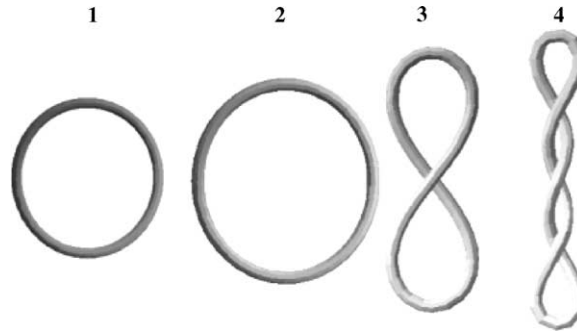


Fig. 8. Shape of the growing loop for $\tau_0 R_0 = 10.0$, $\Omega_3(t = 0) = 8.3$, and $\sigma_{t_{\text{bend}}} = 0.1$ at (1) $t/t_{\text{bend}} = 0.03$, (2) $t/t_{\text{bend}} = 2.41$, (3) $t/t_{\text{bend}} = 3.22$, and (4) $t/t_{\text{bend}} = 3.37$.

$\sigma_{t_{\text{bend}}} = 0.1$. For early times (Fig. 8(1)), the circular loop is stable and perturbations decay. As the loop grows, R increases exponentially and Ω_3 decreases. At a critical value of Ω_3 and R (Fig. 8(2)), the loop begins to buckle and wrap about itself. For sufficiently large $\tau_0 R_0$, the loop takes on the conformation of a *plectoneme*, initially forming a figure-eight structure (Fig. 8(3)) and then wrapping into a braided form (Fig. 8(4)). Fig. 9 shows the twist energy, $\int C(\Omega_3 - \tau_0)^2/2 ds$, and bend energy, $\int A\kappa^2/2 ds$, for the growing loop depicted in Fig. 8. Note that the total energy is not fixed in our model since growth acts to inject energy into the system. At point 1 in Fig. 9, growth along the filament axis leads to a decrease of twist in time and thus an increase in the twist energy. At the same time, backbone perturbations die away and the curvature decreases exponentially, leading to a decrease in the bend energy. At point 2, the circular loop becomes observably unstable. The bend energy begins increasing as perturbations in the filament grow, and the twist energy continues increasing (see Fig. 9). At the inflection point, point 3, the filament forms a figure-eight pattern. Note that a figure-eight shape of a closed loop which is not growing is a minimum of the total energy for a range of twist. At later times (such as point 4), the filament wraps into a braided structure. The bend energy increases as more braids are added. The twist energy also increases; however, writhing motions act to decrease the twisting stress imposed by growth, leading to a twist energy that grows sub-exponentially (see Fig. 9).

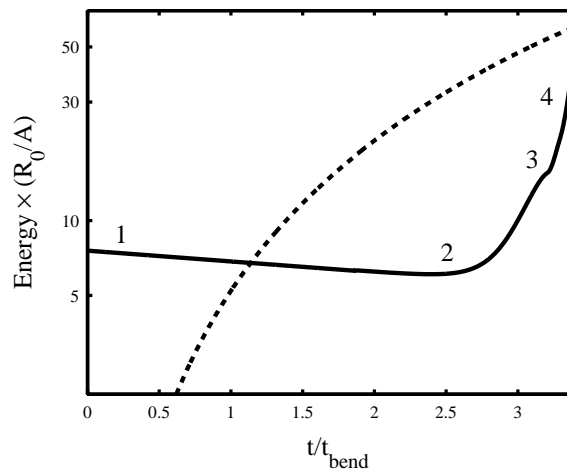


Fig. 9. Semi-log plot of the bend (solid line) and twist (dashed line) energy vs. time. Numbers correspond to shapes in Fig. 8 and label important times during growth (see text for further explanation).

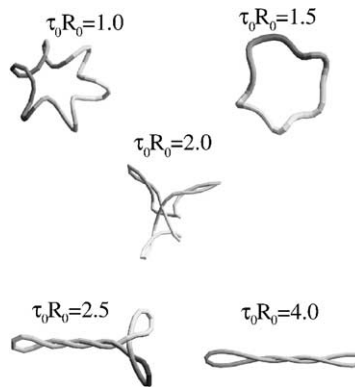


Fig. 10. Morphology of the growing loop at different values of $\tau_0 R_0$. Solenoidal morphologies occur when $\tau_0 R_0 < 2$. Branched plectonemes are observed for $2 \leq \tau_0 R_0 \leq 3$ and unbranched plectonemes are observed when $\tau_0 R_0 > 4$. $\sigma t_{\text{bend}} = 0.01$ for all figures.

The dynamic equations were solved for a range of $\tau_0 R_0$ and σt_{bend} . When $\tau_0 R_0$ was larger than about 4–10 (the actual value depended on the value of σt_{bend}), we found plectonemes. Smaller values of $\tau_0 R_0$ yielded solenoids. Fig. 10 shows how the morphology of the loop depends on the value of $\tau_0 R_0$ at fixed σt_{bend} . In the region with plectonemes, the shapes form as a result of a writhing instability; the Euler-like buckling instability [29–31] plays little role. In particular, the braided shapes remain after growth ceases. Thus, the shapes are qualitatively similar to the minimizers of the elastic energy without growth. However, as discussed in Section 3.3, the rate of growth affects the shape since the number of branches increases with σt_{bend} . In the region with solenoids, the Euler-like buckling instability comes into play since the small value of $\tau_0 R_0$ delays the onset of the writhing instability. Solenoids are not minimizers of the elastic energy without growth; when growth ceases the solenoids relax. Therefore, the solenoids are the three-dimensional analogs of the two-dimensional shapes of references [29–31]. The plectonemic,

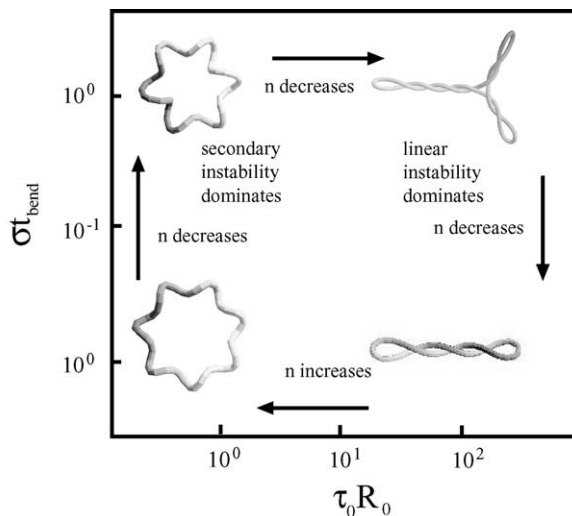


Fig. 11. Qualitative phase diagram depicting the dominant mode behavior as a function of σt_{bend} and $\tau_0 R_0$. For $\tau_0 R_0$ greater than roughly 10, the linear stability analysis predictions are valid and the $n = 2$ and 3 modes dominate the pattern formation. At lower values of $\tau_0 R_0$, a secondary instability drives pattern selection and higher order modes dominates. Insets show the morphology of the loop in different regions of the diagram.

three-armed, and solenoidal morphologies we obtain are similar to many of the supercoiled patterns that are observed in *B. subtilis*; in the conclusion we discuss the relation between our results and the experiments.

In these calculations, we defined the time to the onset of the instability as the point where the bend energy begins increasing (point 2 in Fig. 9). This time should correspond roughly to t_2 defined in Section 3.3, since the perturbations must be noticeably large before they affect the bending energy. Just as in the linear stability analysis, increasing $\tau_0 R_0$ or σ reduces the time to onset of the instability. For values of $\tau_0 R_0 \geq 10$, the time to onset found numerically was in quantitative agreement with the linear stability analysis (see Fig. 6). At smaller values of $\tau_0 R_0$ the onset time from the simulations was earlier than that predicted by the linear analysis, with the deviation getting larger for decreasing σt_{bend} . The deviation is due to a secondary instability: before the growing $n = 2$ mode becomes observably large, it is overtaken by a higher order mode which quickly dominates the shape of the loop. The value of the mode that dominates depends on the value of σt_{bend} and $\tau_0 R_0$. As $\tau_0 R_0$ is decreased at constant σt_{bend} , the mode that dominates increases. As σt_{bend} is increased at constant $\tau_0 R_0$, the mode that dominates decreases. Fig. 11 shows the phase diagram and examples of plectonemes and solenoids. As a check, we verified the secondary instability by discretizing the full nonlinear equations (32)–(34), and integrating with the MATLAB routine ode15s (a variable order, variable time step method for stiff problems).

4. Conclusions

The three essential elements of any growth process appear in our model for *B. subtilis* fibers in a simple form: the mode of growth is exponential extension with rotation, the material properties are described by the bending and twisting elasticity of a slender filament, and the interaction with the external environment is governed by resistive-force theory. Thus, our model is ideal for illustrating the basic phenomena of the physics of growth. We have assumed that the bacterial filaments can be treated as perfectly elastic and that the growth rates are uniform and independent of stress. The degree to which these simplifying assumptions hold remains an outstanding experimental problem. Furthermore, our model does not lead to plectonemic structures for the case of bacterial fibers with free ends for the measured values of the growth parameters and elastic moduli. Nevertheless, we can draw some general conclusions from our model and use our results to suggest new mechanisms for pattern formation in the presence of biological growth.

First, even though the ultimate microscopic mechanism for the supercoiled patterns of *B. subtilis* fibers is unknown, the blocked rotation mechanism we study here must play a role in the supercoiling of closed fibers. For example, since the closed loops form supercoils at lengths which are much shorter than the length at which the open fibers supercoil [19], we expect that the blocked rotation mechanism dominates over whatever mechanism causes the open fibers to supercoil. Thus, we can directly compare our calculations with the experiments on the supercoiling of closed filaments. Recalling the parameters of Section 3.1, we estimate $\sigma t_{\text{bend}} \ll 1$, so that we expect unbranched plectonemes when $\tau_0 R_0 \gtrsim 4$, branched plectonemes when $2 \lesssim \tau_0 R_0 \lesssim 4$, and solenoids when $\tau_0 R_0 \lesssim 2$. Typical observations of the filaments yield unbranched plectonemes, but branched plectonemes and solenoids also arise, depending on the growth medium. Using the observed buckling radius for an unbranched plectoneme, in Section 3.1 we were able to estimate $\tau_0 \approx 10^4 \text{ cm}^{-1}$, suggesting the presence of a structure in the cell wall with pitch $P \approx 10^{-4} \text{ cm}$. The observations of helical actin-like polymers in the cell wall with comparable pitch [51] support our estimate, and further suggests a starting point for a theory for the microscopic mechanism of the supercoiling.

The second major conclusion of our work is the dynamical nature of the pattern selection. For large $\tau_0 R_0$, the plectonemes remain once growth ceases, and are qualitatively similar to the minimizers of the elastic energy, although the rate of growth plays an important role in determining the shape. For small $\tau_0 R_0$, the solenoids are transient structures which relax away when growth halts. Since the curvature of the bacterial fibers can become

permanent [26], the solenoidal shapes may act as a template for patterns which remain in the absence of growth. This mechanism of pattern formation via the hardening of transient structures formed from the interplay of flexibility and external friction may apply to other biological systems, such as those studied in [31].

To help justify, refine, or rule out our model, we suggest three basic experiments. First, the shape of a growing loop as function of time should be measured precisely enough to compare with our theory. Although our numerical results (Fig. 8) are qualitatively similar to the experimentally observed shapes (Fig. 1), the lack of detailed information about the evolution in time of a single loop in [18] prevents a stringent test of our theory. Second, the change in elastic properties with time during growth should be quantitatively measured. For example, to what degree and how long must a fiber be bent to develop a permanent curvature? Finally, the nature of the twist stress in a growing fiber with free ends should be determined. Is there a twist moment on the cross-sections of the growing fibers with free ends, leading to a writhing mechanism qualitatively similar to the blocked rotation mechanism for closed loops, or is the mechanism for open fibers completely different? Future progress toward understanding the pattern formation of *B. subtilis*, both at the microscopic level of the structure of the cell wall and the more macroscopic level treated here, depends critically on new experiments such as these.

Acknowledgements

We thank K. Breuer, D. Coombs, A. Goriely, M. Kim, and C.H. Wiggins for useful discussions. We are particularly grateful to N.H. Mendelson for discussions and the micrograph of Fig. 1, and A. Goriely for alerting us to Refs. [48,49]. CWW was partially supported by the NSF Postdoctoral Fellowship in Microbial Biology. REG acknowledges support from NSF DMR-9812526; TRP acknowledges support from NSF CMS-0093658.

References

- [1] D.W. Thompson, *On Growth and Form*, Cambridge University Press, Cambridge, 1992.
- [2] C. Darwin, *The Movements and Habits of Climbing Plants* D, 2nd ed., Appleton and Co., New York, 1888.
- [3] A. Goriely, M. Tabor, *Phys. Rev. Lett.* 80 (1998) 1564.
- [4] J.A. Warren, J.S. Langer, *Phys. Rev. E* 47 (1993) 2702.
- [5] A.J. Dickstein, S. Erramilli, R.E. Goldstein, D.P. Jackson, S.A. Langer, *Science* 261 (1993) 1012.
- [6] D.P. Jackson, R.E. Goldstein, A.O. Cebers, *Phys. Rev. E* 50 (1994) 298.
- [7] N.R. Lebovitz, A.I. Pesci, *SIAM J. Appl. Math.* 55 (1995) 1117.
- [8] N.H. Mendelson, *Microbiol. Rev.* 46 (3) (1982) 341.
- [9] A.L. Koch, *Appl. Environ. Microbiol.* 66 (9) (2000) 3657.
- [10] R.E. Maxwell, V.S. Nickel, *Science* 120 (1954) 270.
- [11] C.P. Wolk, Y. Cai, J.M. Panoff, *Proc. Natl. Acad. Sci. USA* 88 (1991) 5355.
- [12] H. Sun, Z. Yang, W. Shi, *Proc. Natl. Acad. Sci. USA* 96 (1999) 15178.
- [13] S. Attorri, S. Dunbar, J.E. Clarridge III, *J. Clin. Microbiol.* 38 (2000) 1426.
- [14] G.D. Anagnostopoulos, H.S. Sidhu, *Microbios. Lett.* 5 (1979) 115.
- [15] P.H. Janssen, L.E. Parker, H.W. Morgan, *Antonie van Leeuwenhoek* 59 (1991) 147.
- [16] W. Hernandez-Muniz, S.E. Stevens Jr., *J. Bacteriol.* 170 (1988) 1519.
- [17] M.J. Tilbey, *Nature* 266 (1977) 450.
- [18] N.H. Mendelson, *Proc. Natl. Acad. Sci. USA* 73 (1976) 1740.
- [19] N.H. Mendelson, J.J. Thwaites, J.O. Kessler, C. Li, *J. Bacteriol.* 177 (1995) 7060.
- [20] L.J. Jones, R. Carballido-Lopez, J. Errington, *Cell* 104 (2001) 913.
- [21] S. Ben-Yehuda, R. Losick, *Cell* 109 (2002) 257.
- [22] S. Thitamadee, K. Tuchiya, T. Hashimoto, Private communication.
- [23] N.H. Mendelson, Private communication.
- [24] N.H. Mendelson, D. Favre, J.J. Thwaites, *Proc. Natl. Acad. Sci. USA* 81 (1984) 3562.
- [25] N.H. Mendelson, D. Favre, *J. Bacteriol.* 169 (1987) 519.

- [26] N.H. Mendelson, P. Shipman, D. Roy, L. Chen, J.J. Thwaites, The dynamic behavior of bacterial macrofibers growing with one end prevented from rotating: shaft rotation along the fiber's length, and supercoil migration on a solid surface toward the constrained end, Preprint, 2003.
- [27] K. Larson, *Am. J. Bot.* 87 (2000) 533.
- [28] N.H. Mendelson, J.E. Sarlls, C.W. Wolgemuth, R.E. Goldstein, *Phys. Rev. Lett.* 84 (2000) 1627.
- [29] M.J. Shelley, T. Ueda, The nonlocal dynamics of stretching, buckling, filaments, in: D.T. Papageorgiou, Y.Y. Renardy, A.V. Coward, S.-M. Sun (Eds.), *Advances in Multi-fluid Flows*, SIAM, Philadelphia, PA, 1996.
- [30] M.J. Shelley, T. Ueda, *Physica D* 146 (2000) 221.
- [31] D. Drasdo, *Phys. Rev. Lett.* 84 (2000) 4244.
- [32] I. Klapper, *J. Comp. Phys.* 125 (1995) 325.
- [33] A. Goriely, M. Tabor, *Nonlin. Dyn.* 21 (2000) 101.
- [34] G. Kirchhoff, *J.F. Math (Crelle)* 50 (1859) 285.
- [35] L.D. Landau, E.M. Lifshitz, *Theory of Elasticity*, 3rd ed., Pergamon Press, Oxford, 1986.
- [36] F. Frenet, *J. de Mathém.* 17 (1852) 437.
- [37] J.A. Frenet, *J. de Mathém.* 16 (1851) 193.
- [38] R.D. Kamien, *Rev. Mod. Phys.* 74 (2002) 953.
- [39] J. Fein, *Can. J. Microbiol.* 26 (1980) 330.
- [40] A.L. Koch, *Arch. Microbiol.* 153 (1990) 569.
- [41] C.W. Wolgemuth, T.R. Powers, R.E. Goldstein, *Phys. Rev. Lett.* 84 (2000) 1623.
- [42] R.E. Goldstein, A. Goriely, G. Huber, C.W. Wolgemuth, *Phys. Rev. Lett.* 84 (2000) 1631.
- [43] I. Klapper, M. Tabor, *Physica A* 27 (1994) 4919.
- [44] A.E.H. Love, *A Treatise on the Mathematical Theory of Elasticity*, 4th ed., Dover, New York, 1944.
- [45] J.B. Keller, S.I. Rubinow, *J. Fluid Mech.* 75 (1976) 705.
- [46] L.E. Becker, S.A. Koehler, H.A. Stone, *J. Fluid Mech.* 490 (2003) 15.
- [47] R.L. Bishop, *Am. Math. Monthly* 82 (1975) 246.
- [48] J. Michell, *Messenger Math.* 19 (1889–1890) 181.
- [49] A.B. Basset, *Am. J. Math.* 17 (1895) 281.
- [50] E.E. Zajac, *Trans. ASME* 29 (1962) 136.
- [51] L.J.F. Jones, R. Carballido-López, *J. Errington. Cell* 104 (2001) 913.
- [52] R.E. Goldstein, T.R. Powers, C.H. Wiggins, *Phys. Rev. Lett.* 80 (1998) 5232.
- [53] P.G. Drazin, W.H. Reid, *Hydrodynamic Stability*, Cambridge University Press, Cambridge, 1981.
- [54] P.J. Schmid, D.S. Henningson, *Stability and Transition in Shear Flows*, Springer-Verlag, New York, 2001.
- [55] P.J. Schmid, *Phys. Plasmas* 7 (2000) 1788.
- [56] G. Strang, *Linear Algebra and Its Applications*, 3rd ed., Harcourt, Brace and Jovanovich, San Diego, 1988.
- [57] D.J. Higham, N.J. Higham, *MATLAB Guide*, SIAM, Philadelphia, PA, 2000.
- [58] A. Messiah, *Quantum Mechanics*, vol. II, North-Holland, Amsterdam, 1966.
- [59] R.E. Goldstein, D.P. Jackson, *J. Phys. Chem.* 98 (1994) 9626.